Strong-field-induced N_2^+ lasing by phase control of free induction decay

Siqi Wang,[1] Yao Fu,[1,*] Erik Lötstedt,[2] Jincheng Cao,[1] Hongwei Zang,[1] Helong Li,[1,3] Kaoru Yamanouchi,[2,†] and Huailiang Xu[1,‡]

[1]*State Key Laboratory of Integrated Optoelectronics, College of Electronic Science and Engineering, Jilin University, Changchun 130012, China*

[2]*Department of Chemistry, School of Science, The University of Tokyo, 7-3-1 Hongo, Bunkyo-ku, Tokyo 113-0033, Japan*

[3]*Institute of Atomic and Molecular Physics, Jilin University, Changchun 130012, China*

(Received 26 April 2023; revised 24 July 2023; accepted 7 September 2023; published 26 September 2023)

We prepare N_2^+ mostly in the vibrational ground $X^2\Sigma_g^+$ state by an ultraviolet 267-nm pulse and create the free induction decay (FID) of the $B^2\Sigma_u^+ - X^2\Sigma_g^+(0, 0)$ transition at 391 nm by a resonant excitation pulse. By controlling the phase shift of the FID using a near-IR control pulse through the dynamical Stark effect and rotational coherence, we reveal that the absorption spectrum of this transition, exhibiting a Lorentzian absorption profile, can be changed into a Fano-type profile, and then, a Lorentzian emission profile, resulting in N_2^+ lasing. Our results shed light on the long-term controversy over the mechanism of strong-field-induced N_2^+ lasing and reveal a general route to achieving amplification of light resonantly interacting with molecular ions without population inversion.

DOI: 10.1103/PhysRevA.108.033113

I. INTRODUCTION

Generation of coherent and unidirectional light beam remotely in air has been anticipated for a variety of applications such as spectroscopy [1,2], sensing [3,4], and material processing [5,6]. Recent advances in strong laser technologies have made it possible to generate such air lasers by a cavity-free scheme [7–13]. With the strong-field pumping of N_2 [7–12] and O_2 [13] in the air, high-gain coherent radiations have been observed in both backward and forward propagation directions. In particular, special attention has been paid to the $B^2\Sigma_u^+ - X^2\Sigma_g^+$ (0, 0) lasing emission of N_2^+ at 391 nm induced by intense near-IR laser pulses [10–12,14–20] because of the external controllability of its population transfer among the three lowest-lying electronic states of $X^2\Sigma_g^+$, $A^2\Pi_u$, and $B^2\Sigma_u^+$ via a variety of possible processes such as postionization coupling [14–19] and field-induced recollision [20] after the multiple photon ionization and/or tunnel ionization of N_2 [21,22]. On the other hand, whether the optical gain at 391 nm is ascribed to the population inversion between the $X^2\Sigma_g^+$ ($\upsilon'' = 0$) and $B^2\Sigma_u^+$ ($\upsilon = 0$) states of N_2^+ has been a controversial issue in the past decades [14,15,20,23,24].

In the present study, we prepare N_2^+ mostly in the vibrational ground $X^2\Sigma_g^+$ state by an ultraviolet 267-nm pulse and report an experimental demonstration of coherent control of the absorption line profile of the resonant $B^2\Sigma_u^+ - X^2\Sigma_g^+(0, 0)$ transition by manipulating the phase of the free induction decay (FID) of N_2^+. It has been reported that, if excitation light is resonant with the optical transitions of an absorptive medium, the resultant absorption profile can change depending on the phase shift of the photoemission through the FID of the excited atoms/molecules with respect to the resonant excitation pulse by the Stark effect in atoms [25,26] or rotational coherence in molecules [27]. However, these experimental studies were performed mostly with neutral atoms/molecules by spatiotemporal manipulation of the excitation light in a weak field regime so that the ionization does not occur. Moreover, coherent control of FID phase in molecules through the Stark shift has not been reported probably because the spectral lines are broadened inhomogeneously to a certain extent by the overlap of rovibronic transition peaks. Here we demonstrate the phase control of FID in N_2^+ cation in an intense laser field and reveal straightforwardly that the absorption line profile of N_2^+ can be changed from a Lorentzian profile into an asymmetric Fano profile and then into an inverted Lorentzian profile, representing the optical gain. We experimentally confirm that the change in the spectral line shape of the resonant $B^2\Sigma_u^+ - X^2\Sigma_g^+(0, 0)$ transition in N_2^+ originates from the dynamic Stark effect and the rotational coherence. Our approach to the FID phase control of molecular ions by the resonant excitation laser pulse shows a feature different from previous reports on N_2^+ lasing [10–12,14–20] and provide an opportunity to control FID signals coherently at sufficiently high light field intensity.

II. EXPERIMENTAL SETUP AND BASIC PRINCIPLE

The experimental setup is depicted in Fig. 1(a). The near-IR (800 nm) laser output of the Ti:sapphire laser system (Spectra Physics, Spitfire ACE) with a repetition rate of 200 Hz was first frequency-doubled in a β-barium borate (BBO) crystal having a thickness of 200 μm and a diameter of 10 mm. The generated second harmonic (400 nm) was then

*yaofu@jlu.edu.cn
†kaoru@chem.s.u-tokyo.ac.jp
‡huailiang@jlu.edu.cn

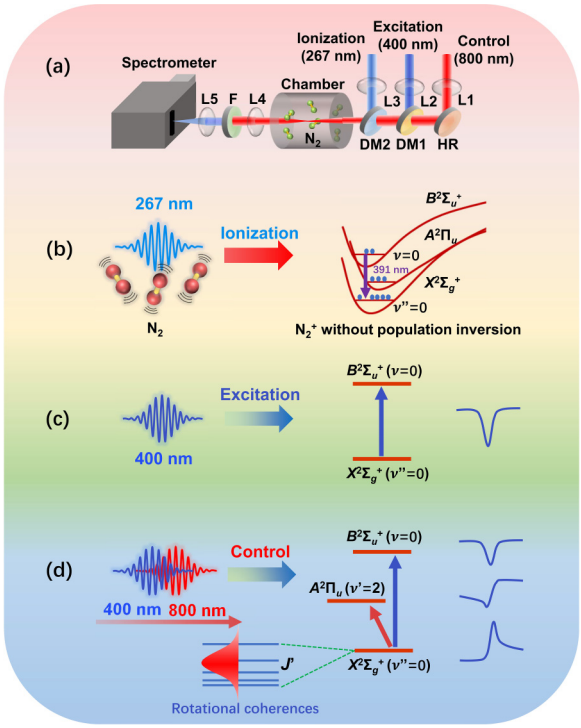

FIG. 1. Experimental setup and schematic scheme for the coherent control of the transient absorption of N_2^+ in an intense pulsed laser field. (a) Experimental setup. L: fused silica lens; HR: mirror with high reflectivity at 800 nm; DM1: mirror with high reflectivity at 400 nm and high transmission at 800 nm; DM2: mirror with high reflectivity at 267 nm and high transmission at 400 nm and 800 nm; F: filter. (b) Non-population-inverted N_2^+ prepared by the ionization of N_2 using an intense 267-nm ionization pulse. (c) Symmetric Lorentzian absorption profile for the $B^2\Sigma_u^+ - X^2\Sigma_g^+(0, 0)$ transition probed by a 400-nm excitation pulse, and (d) the modulated absorption and emission line shapes influenced by an 800-nm control pulses.

separated from the fundamental near-IR light by a dichroic mirror with high reflectivity at 400 nm and high transmission at 800 nm. The near-IR laser beam passed through a temporal delay line (Thorlabs) and was then combined with the second harmonic by another dichroic mirror. The combined beam was used to generate an ionization laser pulse (267 nm, 0.85 mJ) through the sum frequency in another BBO crystal with a thickness of 440 μm and a diameter of 10 mm. The remaining second harmonic pulse was attenuated by a dichroic mirror, producing an excitation pulse having the pulse energy of 1.5 μJ. The remaining near-IR laser pulse was attenuated using a half wave plate and a polarizer, producing a control pulse (800 nm) having a pulse energy in the range 100–500 μJ. The pulse durations of the ionization (267 nm), excitation (400 nm), and control (800 nm) pulses were about 160 fs. The polarization directions of all the ionization, excitation, and control pulses were set to be parallel to each other. The ionization, excitation, and control beams were focused respectively by fused silica lenses whose focal length are $f = 10$ cm (L1), 15 cm (L2), and 20 cm (L3), and then combined by two dichroic mirrors (DM1 and DM2) collinearly before being introduced into a chamber filled with a nitrogen gas at 20 mbar. The time delays among the three pulses were controlled by two motorized delay stages (Newport) with temporal resolution of ∼10 fs, that is, one in the excitation beam line and the other in the control beam line. The laser pulses exiting from the gas chamber were first collimated by a $f = 15$ cm (L4) fused silica lens. The light pulses at 400 nm separated by a filter (F) were then focused by a fused silica focal lens (L5: $f = 6$ cm) into a grating (1800-grooves/mm) spectrometer (Andor Shamrock SR-303i) coupled with an intensified charge-coupled detector (ICCD) camera (Andor iStar) whose gate delay and gate width were set to −5 and 50 ns, respectively. All the spectral data were accumulated over 1000 laser shots.

Figures 1(b) and 1(c) show a schematic diagram of our experimental scheme. In the pump step [Fig. 1(b)], the 267-nm laser pulse ionizes N_2 to generate N_2^+ whose populations in the $B^2\Sigma_u^+$ ($\upsilon = 0$) and $X^2\Sigma_g^+$ ($\upsilon'' = 0$) states are not inverted. Hereafter this pump laser is called the ionization pulse. In the resonant excitation step [Fig. 1(c)], the broadband 400-nm pulse, covering the $B^2\Sigma - X^2\Sigma_g^+$ (0, 0) transition at 391 nm, prepares a coherent superposition of the $X^2\Sigma_g^+$ ($\upsilon'' = 0$) and $B^2\Sigma_u^+$ ($\upsilon = 0$) states of N_2^+ by resonant excitation, creating the FID signal. The interference between the excitation pulse and the FID at the resonant frequency can be monitored by the spectral profile of the absorption peak, which varies sensitively depending on the shift of the FID phase φ with respect to the phase of the excitation pulse [25–27]. The relation between the spectral profile of the absorption peak and the shift of the FID phase φ can be interpreted as follows. The profile of the absorption cross section $\sigma(E)$ of the spectral line with E being the photon energy $E = \hbar\omega$ is known to vary as a function of the Fano parameter q as [28]

$$\sigma(E) = \sigma_0 \frac{(q+\varepsilon)^2}{1+\varepsilon^2}, \tag{1}$$

where

$$\varepsilon = \frac{(E - E_0)}{\hbar(\Gamma/2)} \tag{1.1}$$

and E_0 ($=\hbar\omega_0$) and Γ are the energy and width of the resonant electronic transition, respectively. The absorption cross section $\sigma(E)$ is related to the imaginary part of the polarizability, and thus, to the imaginary part of the frequency-domain dipole response function $d(E)$ as $\sigma(E) \propto \mathrm{Im}\,[d(E)]$. By the Fourier transform, $d(E)$ can be related to the FID, $D(t)$, as [28]

$$D(t) = \frac{1}{2\pi}\int_{-\infty}^{+\infty} d\omega d\left(\frac{\omega - \omega_0}{\Gamma/2}\right) e^{i\omega t}. \tag{2}$$

Therefore, the Fano parameter q can be related to the phase shift $\Delta\varphi$ of FID as [25]

$$\Delta\varphi(q) = 2\arg(q - i), \text{ or } q(\Delta\varphi) = -\cot\left(\frac{\Delta\varphi}{2}\right). \tag{3}$$

Accordingly, the symmetric Lorentzian absorption line shape at $\Delta\varphi = 2m\pi$ with m being an integer corresponds to $q \to \infty$. While $\Delta\varphi = (2m+1)\pi$ (i.e., $q = 0$) results in a negative symmetric Lorentzian absorption line shape, i.e., a symmetric Lorentzian emission line shape [25]. At any other $\Delta\varphi$ values, an asymmetric Fano line profile is formed.

In general, without the perturbation by an external field, the phase shift between the FID and the excitation pulse is

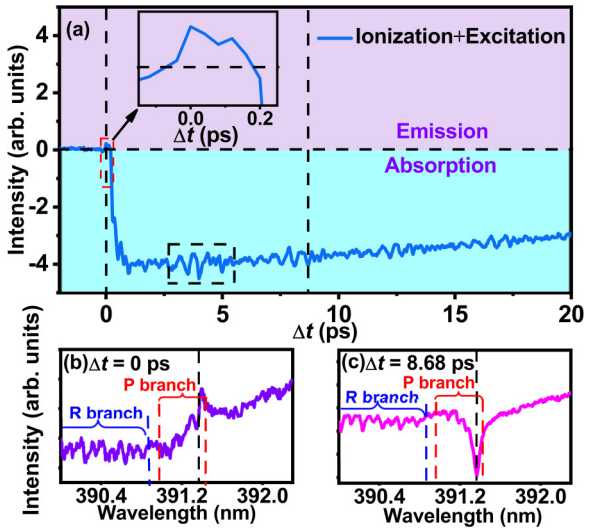

FIG. 2. (a) The measured intensity of the excitation pulse at 391.37 nm matching the wavelength of the $B^2\Sigma_u^+ - X^2\Sigma_g^+$ (0, 0) transition of N_2^+ as a function of the time delay (Δt) between the ionization pulse (267 nm) and the excitation pulse (400 nm). Inset in (a): An expanded view of the intensity profile at $\Delta t \sim 0$ ps. (b), (c) Typical emission (b) and absorption (c) spectral profiles at $\sim$ 391 nm.

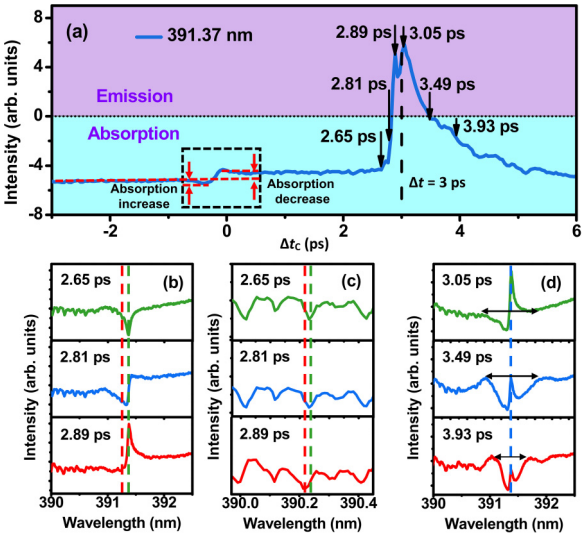

FIG. 3. (a) The spectral line profiles of the $B^2\Sigma_u^+ - X^2\Sigma_g^+(0, 0)$ transition of N_2^+ at 391.37 nm as a function of the time delay (Δt_C) between the ionization (267 nm) and control (800 nm) pulses. The time delay of the excitation pulse from the ionization pulse was fixed at $\Delta t = 3$ ps. (b), (c) The P-branch (b) and R-branch (c) spectra recorded at $\Delta t_C = 2.65$, 2.81, and 2.89 ps. (d) The P-branch spectra recorded at $\Delta t_C = 3.05$, 3.49, and 3.93 ps.

$\Delta\varphi = 2m\pi$, and the absorption spectrum exhibits a symmetric Lorentzian shape as shown in Fig. 1(c). We then introduce the 800-nm pulse as a control pulse to modulate the phase shift $\Delta\varphi$ through the dynamic Stark effect [25,26] and the rotational coherence [27], which can change the absorption profile into an asymmetric Fano line shape as shown in Fig. 1(d), according to Eq. (3). The control pulse can also induce a transfer of the population from the $X^2\Sigma_g^+$ state to the $A^2\Pi_u$ state through the optical coupling [14,15].

III. RESULTS

Figure 2(a) shows the signal intensity of the excitation pulse at 391.37 nm as a function of the time delay (Δt) between the excitation and ionization pulses, in which the positive and negative intensities represent the emission and absorption, respectively. The zero time delay ($\Delta t = 0$) means that the ionization and excitation pulses overlap temporally. As shown in the spectrum taken at $\Delta t = 8.68$ ps [Fig. 2(c)], significant absorption dips are observed not only at the P branch head but also at the R branch transitions of the $B^2\Sigma_u^+ - X^2\Sigma_g^+(0, 0)$ band. This indicates that N_2^+ is prepared by the 267-nm ionization pulse mostly in the electronic ground state, that is, the population inversion between the $X^2\Sigma_g^+$ ($\upsilon'' = 0$) and $B^2\Sigma_u^+$ ($\upsilon = 0$) states is not achieved as schematically shown in Fig. 1(c). In Fig. 2(a), the extent of the absorption decreases gradually after $\Delta t = 600$ fs, which reflects the gradual depletion of the population in the $X^2\Sigma_g^+$ ($\upsilon'' = 0$) state of N_2^+. A periodical baseline oscillation appearing at $\Delta t \sim 4$ ps (surrounded by the dashed rectangle line) can be interpreted as the rotational revival of N_2^+ in the $X^2\Sigma_g^+$ ($\upsilon'' = 0$) state of N_2^+ induced by the ionization pulse. A small positive (emission) peak appearing in the spectrum taken at $\Delta t = 0$ [see the upper left inset in Fig. 2(a)] shows that the lasing emission occurs even when the population inversion is not achieved, exhibiting a marked contrast from the N_2^+ lasing emission created by the 800-nm pump pulse, lasting for a long delay time range between the pump (800 nm) and probe (400 nm) pulses [11,20].

Figure 3(a) shows the variation of the signal intensity at 391.37 nm in the presence of the control pulse (800 nm). In this measurement, Δt is fixed at $\Delta t = 3$ ps as marked by the vertical dashed line in Fig. 3(a) and the control pulse energy is fixed at 200 μJ. Hereafter, the temporal delay between the control and ionization pulses is denoted as Δt_C. In Fig. 3(a), the modulations of the absorption signal intensity can be seen when the control pulse overlaps temporally with the ionization pulse ($\Delta t_C = 0$ ps) as well as when it overlaps temporally with the excitation pulse ($\Delta t_C = 3$ ps). The signal modulation at $\Delta t_C = 0$ (see the area surrounded by the dashed rectangle line) can be attributed to the alignment of N_2 induced by the control pulse, affecting the ionization probability. In addition, the absorption becomes slightly weaker when the control pulse is temporally between the ionization and excitation pulses ($0 < \Delta t_C < 2.6$ ps), which can be ascribed to the population transfer induced by the control pulse from the $X^2\Sigma_g^+$ state to the $A^2\Pi_u$ state of N_2^+ through one-photon resonance absorption, leading to the population decrease in the $X^2\Sigma_g^+$ state [14–19].

When the control pulse is temporally overlapped with the excitation pulse ($\Delta t_C = 3$ ps), the absorption is turned into the emission. Figure 3(b) shows that, when the absorption is turned to the emission, the spectral line shape changes from the symmetric Lorentzian profile to the asymmetric Fano profile, leading to a significant blueshift of the absorption dip. The spectral line-shape change as well as the blueshift of the absorption dip can be seen more clearly in the rotationally resolved R-branch transitions shown in Fig. 3(c). The mod-

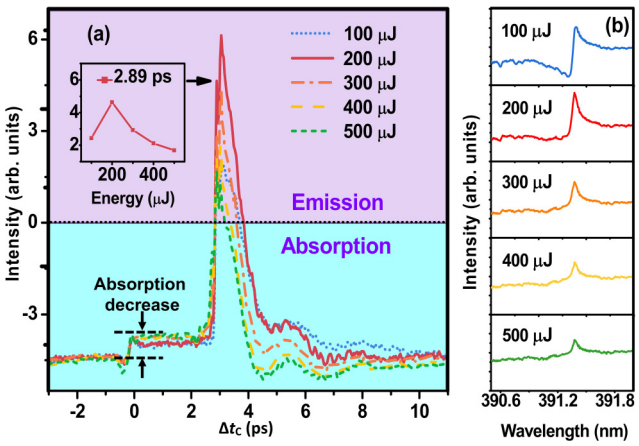

FIG. 4. (a) The intensity of the spectral line at 391.37 nm as a function of the time delay between the pump (267 nm) and control (800 nm) pulses measured at different control pulse energies. The time delay between the pump and excitation pulses was fixed at $\Delta t = 3$ ps. Inset: The variation in the signal intensities measured at the time delay of $\Delta t_C = 2.89$ ps. (b) The *P*-branch spectrum measured at $\Delta t_C = 2.89$ ps at five different laser energies.

ulation in the spectral profile can also be seen at ∼388 nm matching the wavelength of the $X^2\Sigma_g^+$ $(\upsilon'' = 1) - B^2\Sigma_u^+$ $(\upsilon = 1)$ transition as shown in Fig. 6.

The emission reaches the maximum intensity at $\Delta t_C \sim 3$ ps and then decreases slowly as Δt_C further increases as shown in Fig. 3(a). The spectral line profiles of the *P*-branch head measured at the three different Δt_C values in Fig. 3(d) show that the emission peak does not show a frequency shift in this temporal range and that, as Δt_C increases to reach 3.49 and 3.93 ps, the intensity of the Fano profile becomes weaker and the absorption line shape appears more clearly with the narrower linewidth [see the horizontal double arrows in Fig. 3(d)].

We also measure the intensity variation of the spectral signal at 391.37 nm at the different control pulse energies while keeping the time delay at $\Delta t = 3$ ps. As shown in Fig. 4(a), as the control pulse energy increases, the absorption becomes weaker in the delay time range $0 < \Delta t_C <\sim 2.65$ ps, which confirms that the $A^2\Pi_u - X^2\Sigma_g^+$ transition can efficiently deplete the population in the $X^2\Sigma_g^+$ states. On the other hand, when the control and excitation pulses temporally overlap ($\Delta t_C = 3$ ps), the emission intensity first increases and then decreases. The inset in Fig. 4(a) shows the variation of the emission intensity measured at $\Delta t_C = 2.89$ ps, where the maximum intensity occurs at the control pulse energy of 200 μJ. The increase in the control pulse energy also induces the change in the spectral line profile from the asymmetric Fano profile to the symmetric Lorentzian profile as shown in Fig. 4(b).

IV. DISCUSSION

To interpret the above observations, we first examine the mechanism of the switching between the emission and the absorption seen in the two-pulse experiments (Fig. 2). The symmetric Lorentzian absorption line profile obtained in the time delay range after $\Delta t \sim 600$ fs indicates that the phase shift of the FID with respect to the excitation pulse is $\varphi = 2m\pi$, so that $q \to \infty$. This means that there is no external perturbation to change the electronic coherence between the $X^2\Sigma_g^+$ $(\upsilon'' = 0)$ and $B^2\Sigma_u^+$ $(\upsilon = 0)$ states created by the excitation pulse, and consequently, the coherence of FID is not influenced by the ionization process of N_2 induced by the ionization pulse in the time delay range $\Delta t > 600$ fs. However, when the two pulses temporally overlap ($\Delta t = 0$), N_2^+ prepared by the central and strongest part of the ionization pulse can interact with the rear part of the same pulse, which induces energy level shift $\Delta E(t)$ of N_2^+ by the dynamic Stark effect [26], and consequently, the phase shift $\Delta\varphi$ of the FID with respect to the excitation pulse according to the relation [25]

$$\Delta\varphi = -\int \frac{\Delta E(t)}{\hbar} dt, \tag{4}$$

where $\Delta E(t)$ depends also on the intensity of the ionization laser field. As seen in Eq. (4), $\Delta\varphi$ can become negative in the temporally rear part of the ionization pulse. This means that the negative $\Delta\varphi$ falls in the range $\Delta\varphi \in (-\pi, 0)$, corresponding to a positive value of q. This will result in an asymmetric Fano line profile with the emission peak at the longer-wavelength side of the Lorentzian absorption dip, which is consistent with the spectrum in Fig. 2(b).

Next, we examine the switching between the emission and the absorption in the three-pulse experiments shown in Fig. 3. Because the effect of the ionization pulse on the changes in the absorption spectrum is negligible in the time delay range $\Delta t > 600$ fs as shown in Fig. 2, the resultant emission taking place at the delay time of around 3 ps can thus be ascribed to the contribution from the control pulse. However, the spectral changes shown in Figs. 3(b) and 3(d) exhibit different behaviors when the control pulse is before and after the excitation pulse at $\Delta t_C \sim 3$ ps. When the control pulse is before the excitation pulse (i.e., $\Delta t_C < \Delta t = 3$ ps), a rotational coherence of N_2^+ in the ground $X^2\Sigma_g^+$ $(\upsilon'' = 0)$ state can be created by the control pulse through the nonadiabatic rotational alignment of N_2^+ [27]. This long-lived rotational coherence in the $X^2\Sigma_g^+$ $(\upsilon'' = 0)$ state can periodically modulate the electronic coherence between the $X^2\Sigma_g^+$ $(\upsilon'' = 0)$ and $B^2\Sigma_u^+$ $(\upsilon = 0)$ states induced by the subsequent excitation pulse, leading to the FID phase shift. In this case, the change in the spectral line profile depends on the change in the extent of the alignment of the N-N molecular axis of N_2^+ [27]. This interpretation is supported by the oscillation in the spectral intensity appearing in the narrow delay time range $2.89 < \Delta t_C < 3.0$ ps shown in Fig. 3(a). It is possible that the rotational coherence induces alternation of the emission and the absorption with the period of the molecular rotation. However, in this time delay range of $2.89 < \Delta t_C < 3.0$ ps, the oscillation signals always appear as emission, which means that besides the rotational coherence, the Stark effect induced by the control pulse also contributes to the change from the absorption profile to the emission profile.

On the other hand, when the control pulse is after the excitation pulse (i.e., $\Delta t_C > \Delta t = 3$ ps), the spectral modulation continues for about several picoseconds, but gradually decreases as Δt_C increases, which may reflect the decay time of the FID. That is, the FID emission is modulated by the control pulse-induced Stark effect at the moment of $\Delta t_C - \Delta t$ after its creation by the excitation pulse. Therefore, as Δt_C

increases, the effect of the dynamic Stark effect is expected to decrease. This is indeed the case shown in Fig. 3(d), where the absorption spectral linewidth measured at $\Delta t_C = 3.93$ ps is narrower than that at $\Delta t_C = 3.49$ ps and the intensity of the asymmetric Fano line profile in the central part of the absorption profile decreases gradually [see the horizontal double arrows in Fig. 3(d)].

The dynamical Stark effect on $\Delta\varphi$ can also explain the results observed in Fig. 4. According to Eq. (4), the negative phase shift can be strongly influenced by the control pulse energy. Therefore, the increase in the energy of the control pulse may transform the absorption line profile from an asymmetric Fano profile ($\Delta\varphi \in ((2m-1)\pi,\ 2m\pi)$) to a Lorentzian emission profile ($\Delta\varphi = (2m-1)\pi$), resulting in the variation in the line profile shown in Fig. 4(b). The observation that the emission intensity does not increase monotonically with the increase in the control pulse energy [see the inset of Fig. 4(a)] may result from the decrease in the population in the $X^2\Sigma_g^+$ ($\upsilon'' = 0$) state through the population transfer via the $X^2\Sigma_g^+ - A^2\Pi_u$ (0, 0) transition. This process is enhanced as the control pulse energy increases, leading to a decrease in the net population in the coherent superposition of the $X^2\Sigma_g^+$ ($\upsilon'' = 0$) and $B^2\Sigma_u^+$ ($\upsilon = 0$) states and weakening the amplitude of the emission Fano line profile. The variation in the emission intensity may originate also from the spatial ununiformity of the Gaussian intensity distribution of the control pulse in the plane perpendicular to the laser propagation direction, leading to a spatial FID phase change by the dynamic Stark effect, and consequently to the modification of the wave front and beam divergence (see Ref. [26]).

In order to model the 800-nm-controlled absorption of a 400-nm laser pulse by N_2^+ and further verify the contribution of the dynamical Stark effect induced by the control pulse for generating N_2^+ lasing without population inversion, we consider a minimal three-state model consisting of the $X^2\Sigma_g^+$ ($\upsilon'' = 0$) state, the $A^2\Pi_u$ ($\upsilon' = 2$) state, and the $B^2\Sigma_u^+$ ($\upsilon = 0$) state. Overall rotation of N_2^+ is neglected. We consider the time-dependent Schrödinger equation (TDSE)

$$i\hbar\frac{d}{dt}\begin{pmatrix} c_{X0}(t) \\ c_{A2}(t) \\ c_{B0}(t) \end{pmatrix} = \begin{pmatrix} \varepsilon_{X0} & d_{X0A2}(t) & d_{X0B0}(t) \\ d_{X0A2}(t) & \varepsilon_{A2} & 0 \\ d_{X0B0}(t) & 0 & \varepsilon_{B0} \end{pmatrix} \times \begin{pmatrix} c_{X0}(t) \\ c_{A2}(t) \\ c_{B0}(t) \end{pmatrix}, \quad (5)$$

where $c_k(t)$ is the time-dependent coefficient of state k, ε_k is the energy of state k, and $d_{X0A2}(t) = -F(t)\sin\theta\mu_{X0A2}$, $d_{X0B0}(t) = -F(t)\cos\theta\mu_{X0B0}$ are the time-dependent $A^2\Pi_u - X^2\Sigma_g^+$ and $B^2\Sigma_u^+ - X^2\Sigma_g^+$ couplings expressed in terms of the laser field $F(t)$, the angle θ between the N-N molecular axis and the polarization direction of the laser field, and the transition dipole moments μ_{jk}. The state energies ($\varepsilon_{A2} - \varepsilon_{X0} \approx 1.58$ eV and $\varepsilon_{B0} - \varepsilon_{X0} \approx 3.17$ eV) are calculated from the Morse potential parameters given in [29], and the transition dipole moments ($\mu_{X0A2} = 0.249$ D and $\mu_{X0B0} = 1.52$ D) are calculated from the transition dipole curves reported in [30,31]. The laser field is expressed as

$$F(t) = F_{ex}^0 \exp\left(-\frac{2\ln 2t^2}{\tau_{ex}^2}\right)\cos(\omega_{ex}t) + F_{ctrl}^0 \exp\left[-\frac{2\ln 2(t-\Delta t_{cex})^2}{\tau_{ctrl}^2}\right]\cos(\omega_{ctrl}t), \quad (6)$$

where F_{ex}^0 and F_{ctrl}^0 are the peak field strengths of the excitation pulse and the control pulse, respectively, τ_{ex} and τ_{ctrl} are the pulse durations (full width at half maximum), ω_{ex} and ω_{ctrl} are the angular frequencies, and Δt_{cex} is the delay between the control pulse and the excitation pulse.

We solve the TDSE (5) from $t = t_i = -10$ ps to $t = 10$ ps with the initial conditions $c_{X0}(t = t_i) = 1$, $c_{A2}(t = t_i) = 0$, and $c_{B0}(t = t_i) = 0$, corresponding to ionization of N_2 into the $X^2\Sigma_g^+$ ($\upsilon'' = 0$) state of N_2^+ by the 267-nm ionization pulse. The interaction of N_2^+ with the 267-nm ionization pulse is not included in the simulation. We calculate the time-dependent dipole moment $D(t)$ created by the motion of the $B^2\Sigma_u^+ - X^2\Sigma_g^+$ wave packet,

$$D(t) = 2\mathrm{Re}[c_{X0}^*(t)c_{B0}(t)\mu_{X0B0}]. \quad (7)$$

The delay-dependent transient absorption response function $S(\omega)$ is defined as [32]

$$S(\omega) = 2\mathrm{Im}[\tilde{D}(\omega)\tilde{F}^*(\omega)], \quad (8)$$

where $\tilde{D}(\omega)$ is the Fourier transform of the induced dipole $D(t)$, and $\tilde{F}^*(\omega)$ is the complex conjugate of the Fourier transform of the laser field $F(t)$. The response function $S(\omega)$ represents the absorption probability at the frequency ω. A negative value of $S(\omega)$ corresponds to the emission and a positive value of $S(\omega)$ to the absorption. To model the final lifetime of the FID, the induced dipole moment $D(t)$ is multiplied by an exponentially decaying function $e^{-t/T}$ with $T = 1$ ps before performing the Fourier transform.

In Fig. 5, we show the negative response function $-S(\omega)$ as a function of the wavelength for three values of the delay time, $\Delta t_{cex} = -500$ fs, 0 fs, and 500 fs. We show the negative of $S(\omega)$ to allow an easier comparison with the experimentally measured spectral line profiles in Fig. 3. Negative values of $-S(\omega)$ correspond to absorption, and positive values of $-S(\omega)$ correspond to emission. In the simulation, we assume the alignment angle of $\theta = 45°$, the pulse durations of $\tau_{ex} = \tau_{ctrl} = 160$ fs, the angular frequencies of $\omega_{ex} = 4.816$ rad/fs (corresponding to a wavelength of $\lambda_{ex} = 391.1$ nm) and $\omega_{ctrl} = 2.355$ rad/fs (corresponding to a wavelength of $\lambda_{ctrl} = 800$ nm), and the peak light field strengths of $F_{ex}^0 = 8.7\times10^{-3}$ V/Å (corresponding to a peak intensity of 1×10^9 W/cm^2) and $F_{ctrl}^0 = 2.7$ V/Å (corresponding to a peak intensity of 1×10^{14} W/cm^2).

We can see clearly in Fig. 5 that the spectral shape of the response function changes as a function of the delay time between the control pulse and the excitation pulse. At $\Delta t_{cex} = -500$ fs, corresponding to the situation in which the 800-nm control pulse comes before the excitation pulse, $-S(\omega)$ has a Lorentzian shape. On the other hand, at $\Delta t_{cex} = 0$ fs, corresponding to the full temporal overlap of the control and excitation pulses, as well as at $\Delta t_{cex} = 500$ fs, corresponding to the situation in which the control pulse

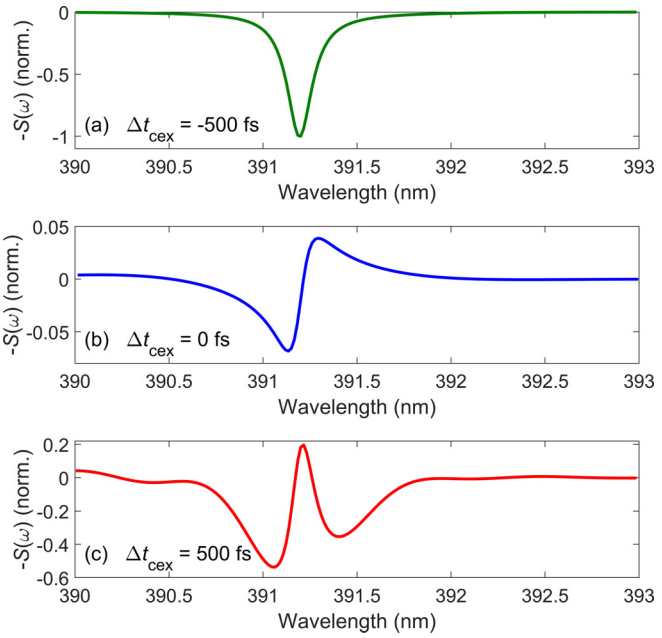

FIG. 5. Negative absorption signal $-S(\omega)$ calculated for the three-level model of N_2^+ exposed to a 391-nm excitation pulse (160 fs, 10^9 W/cm^2) and an 800-nm control pulse (160 fs, 10^{14} W/cm^2). (a) The delay between the 800-nm control pulse and the 391-nm excitation is $\Delta t_{cex} = -500$ fs (the control pulse comes before the excitation pulse). (b) $\Delta t_{cex} = 0$ fs (the control and excitation pulses overlap temporally). (c) $\Delta t_{cex} = 500$ fs (the control pulse comes after the excitation pulse). $S(\omega)$ is normalized so that the maximum of $S(\omega)$ equals 1 in (a). The same normalization scale is applied in all the three panels.

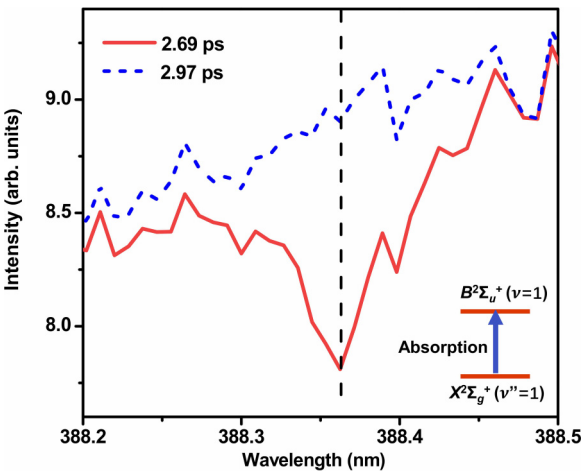

FIG. 6. The spectral profile at ~388.3 nm, corresponding to the $B^2\Sigma_u^+ - X^2\Sigma_g^+(1, 1)$ transition, recorded respectively at the delay time of $\Delta t_C = 2.69$ and 2.97 ps. The time delay between the excitation pulse with respect to the pump pulse was fixed at $\Delta t = 3$ ps and the pulse energy of the control pulse was fixed at 200 μJ.

comes after the excitation pulse, $-S(\omega)$ exhibits an asymmetric Fano profile. The theoretical line profiles in Figs. 5(a)–5(c) reproduce well the recorded experimental line profiles shown in Figs. 3(b) (2.65 ps), 3(d) (3.05 ps), and 3(d) (3.49 ps), respectively. The theoretical simulations demonstrate that the phase shift of the FID can be well explained by the dynamical Stark effect induced by the control pulse.

Finally, in order to verify that the manipulation of the FID phase of molecular ions by the strong-field laser pulse is a universal phenomenon and can be simultaneously triggered at different wavelengths, we measured the spectral band at ~388.3 nm, matching the wavelength of the $B^2\Sigma_u^+ - X^2\Sigma_g^+$ (1, 1) transition of N_2^+ with the three-pulse scheme for the two delay times at $\Delta t_C = 2.69$ ps and 2.97 ps respectively. As shown in Fig. 6, the spectral line at ~388.36 nm shows an absorption profile at $\Delta t_C = 2.69$ ps, which changes into an emission profile at $\Delta t_C = 2.97$ ps in a similar manner as in the case of the spectra shown in Fig. 3(b) for the $B^2\Sigma_u^+ - X^2\Sigma_g^+$ (0, 0) transition at 391.37 nm. However, the contrast of the spectral profile shown in Fig. 6 is lower than that shown in Fig. 3(b). This may be ascribed to the smaller net population in the coherent superposition of the $X^2\Sigma_g^+$ ($\upsilon'' = 1$) and $B^2\Sigma_u^+$ ($\upsilon = 1$) states created by the excitation pulse when compared with that in the coherent superposition of the $X^2\Sigma_g^+$ ($\upsilon'' = 0$) and $B^2\Sigma_u^+$ ($\upsilon = 0$) states [33].

V. CONCLUSIONS

In summary, we have proposed a scheme of manipulating the phase shift of the FID of N_2^+ with respect to the control pulse to control the spectral line profile from a symmetric Lorentzian profile to an asymmetric Fano profile. We have also revealed that both the dynamical Stark effect and the rotational coherence contribute to the FID phase shift of N_2^+ and that the mechanism of the emission of N_2^+ at 391 nm exhibiting the Fano-type emission profiles induced by the near-IR control pulse in the present study is different from the mechanism of the emission of the population-inverted N_2^+ exhibiting a symmetric Lorentzian line shape [10–12,14–20]. We have shown clearly that the emission at 391 nm can be created even when the population inversion is not achieved between the $X^2\Sigma_g^+$ ($\upsilon'' = 0$) and $B^2\Sigma_u^+$ ($\upsilon = 0$) states and demonstrated a general scheme by which coherent emissions at high intensity can be controlled by the FID phase shift in molecular ions.

ACKNOWLEDGMENT

This work was supported in part by the National Natural Science Foundation of China (Grants No. 62027822 and No. 11904121).

[1] J. Kasparian, M. Rodriguez, G. Mejean, J. Yu, E. Salmon, H. Wille, R. Bourayou, S. Frey, Y. B. Andre, A. Mysyrowicz, R. Sauerbrey, J. P. Wolf, and L. Woste, White-light filaments for atmospheric analysis, Science **301**, 61 (2003).

[2] Y. Fu, J. Cao, K. Yamanouchi, and H. Xu, Air-laser-based stand-off coherent Raman spectrometer, Ultrafast Sci. **2022**, 9867028 (2022).

[3] D. K. Killinger and N. Menyuk, Laser remote sensing of the atmosphere, Science **235**, 37 (1987).

[4] H. Xu, Y. Cheng, S. L. Chin, and H. Sun, Femtosecond laser ionization and fragmentation of molecules for environmental sensing, Laser Photon. Rev. **9**, 275 (2015).

[5] Y. Su, S. Wang, D. Yao, Y. Fu, H. Zang, H. Xu, and P. Polynkin, Stand-off fabrication of irregularly shaped, multi-functional hydrophobic and antireflective metal surfaces using femtosecond laser filaments in air, Appl. Surf. Sci. **494**, 1007 (2019).

[6] Y. Su, W. Zhang, S. Chen, D. Yao, J. Xu, X. Chen, L. Liu, and H. Xu, Engineering black titanium dioxide by femtosecond laser filament, Appl. Surf. Sci. **520**, 146298 (2020).

[7] Q. Luo, W. Liu, and S. L. Chin, Lasing action in air induced by ultra-fast laser filamentation, Appl. Phys. B **76**, 337 (2003).

[8] D. Kartashov, S. Alisauskas, G. Andriukaitis, A. Pugzlys, M. Shneider, A. Zheltikov, S. L. Chin, and A. Baltuska, Free-space nitrogen gas laser driven by a femtosecond filament, Phys. Rev. A **86**, 033831 (2012).

[9] A. Laurain, M. Scheller, and P. Polynkin, Low-threshold Bidirectional Air Lasing, Phys. Rev. Lett. **113**, 253901 (2014).

[10] J. Yao, B. Zeng, H. Xu, G. Li, W. Chu, J. Ni, H. Zhang, S. L. Chin, Y. Cheng, and Z. Xu, High-brightness switchable multiwavelength remote laser in air, Phys. Rev. A **84**, 051802 (2011).

[11] J. Yao, G. Li, C. Jing, B. Zeng, W. Chu, J. Ni, H. Zhang, H. Xie, C. Zhang, H. Li, H. Xu, S. L. Chin, Y. Cheng, and Z. Xu, Remote creation of coherent emissions in air with two-color ultrafast laser pulses, New J. Phys. **15**, 023046 (2013).

[12] W. Chu, G. Li, H. Xie, J. Ni, J. Yao, B. Zeng, H. Zhang, C. Jing, H. Xu, Y. Cheng, and Z. Xu, A self-induced white light seeding laser in a femtosecond laser filament, Laser Phys. Lett. **11**, 015301 (2014).

[13] A. Dogariu, J. B. Michael, M. O. Scully, and R. B. Miles, High-gain backward lasing in air, Science **331**, 442 (2011).

[14] H. Xu, E. Lötstedt, A. Iwasaki, and K. Yamanouchi, Sub-10-fs population inversion in N_2^+ in air lasing through multiple state coupling, Nat. Commun. **6**, 8347 (2015).

[15] J. Yao, S. Jiang, W. Chu, B. Zeng, C. Wu, R. Lu, Z. Li, H. Xie, G. Li, C. Yu, Z. Wang, H. Jiang, Q. Gong, and Y. Cheng, Population Redistribution Among Multiple Electronic States of Molecular Nitrogen Ions in Strong Laser Fields, Phys. Rev. Lett. **116**, 143007 (2016).

[16] H. Xu, E. Lötstedt, T. Ando, A. Iwasaki, and K. Yamanouchi, Alignment-dependent population inversion in N_2^+ in intense few-cycle laser fields, Phys. Rev. A **96**, 041401 (2017).

[17] H. Li, M. Hou, H. Zang, Y. Fu, E. Lötstedt, T. Ando, A. Iwasaki, K. Yamanouchi, and H. Xu, Significant Enhancement of N_2^+ Lasing by Polarization-Modulated Ultrashort Laser Pulses, Phys. Rev. Lett. **122**, 013202 (2019).

[18] T. Ando, E. Lötstedt, A. Iwasaki, H. Li, Y. Fu, S. Wang, H. Xu, and K. Yamanouchi, Rotational, Vibrational, and Electronic Modulations in N_2^+ Lasing at 391 nm: Evidence of Coherent $B^2\Sigma_u^+ - X^2\Sigma_g^+ - A^2\prod_u$ Coupling, Phys. Rev. Lett. **123**, 203201 (2019).

[19] H. Li, E. Lötstedt, H. Li, Y. Zhou, N. Dong, L. Deng, P. Lu, T. Ando, A. Iwasaki, Y. Fu, S. Wang, J. Wu, K. Yamanouchi, and H. Xu, Giant Enhancement of Air Lasing by Complete Population Inversion in N_2^+, Phys. Rev. Lett. **125**, 053201 (2020).

[20] Y. Liu, P. Ding, G. Lambert, A. Houard, V. Tikhonchuk, and A. Mysyrowicz, Recollision-induced Superradiance of Ionized Nitrogen Molecules, Phys. Rev. Lett. **115**, 133203 (2015).

[21] X. Tong, Z. Zhao, and C. Lin, Theory of molecular tunneling ionization, Phys. Rev. A **66**, 033402 (2002).

[22] Y. Wang, H. Kang, W. Quan, X. Zhang, Z. Lin, M. Wu, H. Liu, and X. Liu, Multiphoton ionization from multiple orbitals of N_2 in strong laser fields, Chin. Phys. Lett. **27**, 083202 (2010).

[23] A. Mysyrowicz, R. Danylo, A. Houard, V. Tikhonchuk, X. Zhang, Z. Fan, Q. Liang, S. Zhuang, L. Yuan, and Y. Liu, Lasing without population inversion in N_2^+, APL Photon. **4**, 110807 (2019).

[24] M. Richter, M. Lytova, F. Morales, S. Haessler, O. Smirnova, M. Spanner, and M. Ivanov, Rotational quantum beat lasing without inversion, Optica **7**, 586 (2020).

[25] C. Ott, A. Kaldun, P. Raith, K. Meyer, M. Laux, J. Evers, C. H. Keitel, C. H. Greene, and T. Pfeifer, Lorentz meets Fano in spectral line shapes: A universal phase and its laser control, Science **340**, 716 (2013).

[26] S. Bengtsson, E. W. Larsen, D. Kroon, S. Camp, M. Miranda, C. L. Arnold, A. L'Huillier, K. J. Schafer, M. B. Gaarde, L. Rippe, and J. Mauritsson, Space–time control of free induction decay in the extreme ultraviolet, Nat. Photon. **11**, 252 (2017).

[27] P. Peng, Y. Mi, M. Lytova, M. Britton, X. Ding, A. Y. Naumov, P. B. Corkum, and D. M. Villeneuve, Coherent control of ultrafast extreme ultraviolet transient absorption, Nat. Photon. **16**, 45 (2022).

[28] U. Fano and J. W. Cooper, Spectral distribution of atomic oscillator strengths, Rev. Mod. Phys. **40**, 441 (1968).

[29] K. P. Huber, G. H. Herzberg, J. W. Gallagher, and R. D. Johnson, III, Constants of diatomic molecules, in *NIST Chemistry WebBook, NIST Standard Reference Database Number* 69, edited by P. J. Linstrom and W. G. Mallard (National Institute of Standards and Technology, Gaithersburg, MD, 2021).

[30] S. R. Langhoff, C. W. Bauschlicher, Jr., and H. Partridge, Theoretical study of the N_2^+ Meinel system, J. Chem. Phys. **87**, 4716 (1987).

[31] S. R. Langhoff and C. W. Bauschlicher, Jr., Theoretical study of the first and second negative systems of N_2^+, J.Chem. Phys. **88**, 329 (1988).

[32] M. Wu, S. Chen, S. Camp, K. J. Schafer, and M. B. Gaarde, Theory of strong-field attosecond transient absorption, J. Phys. B: At. Mol. Opt. Phys. **49**, 062003 (2016).

[33] Y. Fu, E. Lötstedt, H. Li, S. Wang, D. Yao, T. Ando, A. Iwasaki, F. H. M. Faisal, K. Yamanouchi, and H. Xu, Optimization of N_2^+ lasing through population depletion in the $X^2\Sigma_g^+$ state using elliptically modulated ultrashort intense laser fields, Phys. Rev. Res. **2**, 012007 (2020).